

<https://doi.org/10.1038/s41699-026-00696-z>

Water-based, large-scale transfer of 2D materials grown on sapphire substrates

Check for updates

Nico Rademacher^{1,2,5}, Lukas Völkel^{2,5}, Eros Reato², Martin Otto¹, Simonas Krotkus³, Jan Mischke³, Emre Yengel³, Christof Mauder³, Alex Henning³, Michael Heuken³, Ke Ran^{1,4}, Joachim Mayer⁴ & Max C. Lemme^{1,2} ✉

Two-dimensional materials (2DMs) hold significant potential for future electronics, as demonstrated by high-performing devices for sensing, optics, and electronics. However, scalable growth techniques such as metal-organic chemical vapor deposition (MOCVD) typically require high temperatures, which limit their integration with conventional semiconductor processes. Therefore, reliable transfer processes from crystalline, low-contamination growth substrates such as sapphire are essential. Existing methods using chemicals such as potassium hydroxide (KOH) have potential quality issues and require manual handling and enhanced safety precautions. Here, we introduce a deionized water-based, frame-assisted, large-scale transfer method for two widely used two-dimensional materials, molybdenum disulfide (MoS₂) and hexagonal boron nitride (h-BN). We demonstrate the scalability of our process with the transfer of MoS₂ from a 100 mm diameter sapphire wafer. The material quality was verified as-grown and after transfer via atomic force microscopy, scanning electron microscopy, and Raman spectroscopy. The data show less compressive strain levels and insignificant changes in the doping or contamination of 2DMs after transfer.

High-performance proof-of-concept devices based on two-dimensional materials (2DMs) show great potential for future semiconductor applications in sensing, optoelectronics, and electronics^{1–7}. However, this potential may remain elusive unless 2DMs can be integrated into current semiconductor manufacturing process flows. State-of-the-art 2DM growth with scalable techniques such as metal-organic chemical vapor deposition (MOCVD) is typically not compatible with conventional complementary metal-oxide-semiconductor (CMOS) processes because of high growth temperatures (> 400°C)⁸. Although several groups have recently reported promising approaches to lower the temperature to the desired range^{9,10}, layer transfer remains a promising alternative option, i.e., delaminating the material from the high-temperature growth substrate before bonding it to a target substrate. Sapphire is often used as a growth substrate because of its crystalline nature, chemical inertness, high melting point (2040°C), good thermal conductivity (> 10 W/mK), and controllability of the crystal orientation by a miscut angle (often 0.2°)^{11–13}. Sapphire is also widely used as an epitaxial substrate in the III-V semiconductor industry and, hence, is readily available in standardized wafer formats with sizes of up to 12 inches^{11,14}. 2DM transfer processes from sapphire typically involve the use of chemicals such as potassium hydroxide (KOH). They rely on the skilled

handling of the 2DM during transfer (“fishing transfer”)^{15–18}, with three main steps. First, a protective polymer is spin-coated on top of the 2DM. Second, the 2DM is detached from the growth substrate by holding it manually into a KOH or similar solution at an angle. This step is prone to failure because the researcher must manually maintain the right angle for an extended period. Being close to chemicals also poses a hazard. Third, after the 2DM is detached, the target substrate is submerged in the solution to “fish” out the 2DM film. This is again hazardous and can lead to folding of the 2DM film. Additionally, 2DMs are sensitive to gas-phase and liquid-phase chemicals^{19–21}. For example, KOH can increase the polycrystallinity of the 2DM molybdenum disulfide (MoS₂)¹⁶. This indicates that certain combinations of chemicals and 2DMs should be avoided. Moreover, Zhang et al.²² theoretically investigated the peeling of 2DMs from rigid substrates in a liquid water environment. Their model predicts that interface peeling is promoted in the presence of water molecules when both the 2DM and the substrate are hydrophilic. Surfaces are commonly classified as hydrophilic when the water contact angle (WCA) of a water droplet is below 90°²³, with a lower WCA corresponding to stronger hydrophilicity. Contact angles of ~37°, ~86° and between 52° and 67° have been reported for flat sapphire²⁴, MoS₂²⁵, and hexagonal boron nitride (h-BN)²⁶, respectively. Based on these

¹AMO GmbH, Advanced Microelectronic Center Aachen, Aachen, Germany. ²Chair of Electronic Devices, RWTH Aachen University, Aachen, Germany. ³AIXTRON SE, Herzogenrath, Germany. ⁴Central Facility for Electron Microscopy GFE, RWTH Aachen University, Aachen, Germany. ⁵These authors contributed equally: Nico Rademacher, Lukas Völkel. ✉e-mail: max.lemme@eld.rwth-aachen.de

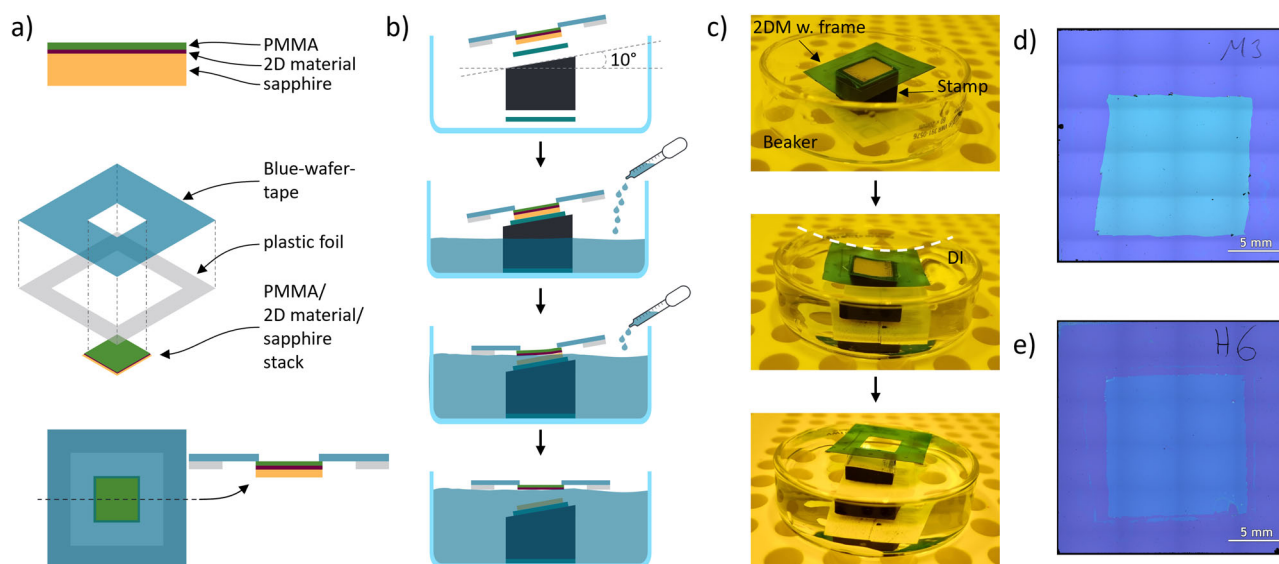


Fig. 1 | Schematic representation of the transfer process. **a** Cross section of the material stack and preparation steps of the supporting plastic foil. **b** Schematic representation of the transfer process from a cross-sectional view. **c** Photographs of the transfer of a MoS₂ piece. Top: Empty beaker with a 3D-printed stamp and MoS₂ with a frame. 2DM for 2DMs. Middle: Beaker half-filled with DI water. The

bending of the frame due to the water tension force is visible. The dashed line serves as a guide to the eye. Bottom: The PMMA/MoS₂ stack with the frame floats on the DI water surface after successful lift-off from the sapphire. Optical microscope images of **(d)** MoS₂ and **(e)** h-BN on a 2 cm × 2 cm Si/SiO₂ chip created via image stitching. The fence-like structure is a stitching artifact.

values, the formation of water/2DM and water/sapphire interfaces is energetically favorable once the 2DM comes into contact with water, thereby promoting interfacial peeling from the sapphire substrate.

Here, we present a large-scale transfer method for the 2DMs MoS₂ and h-BN grown on sapphire. The transfer process utilizes DI water, following the theoretical framework proposed by Zhang et al.²², in combination with a supporting frame that potentially enables enhanced peeling forces and facilitates easier handling of the 2DM films. The absence of acids or bases eliminates their impact on the 2DMs and the hazards of handling them, while the frame stabilizes the fragile 2D films during transfer. Additionally, DI water is environmentally friendly and abundant. We verified the quality of our transfer by atomic force microscopy (AFM), scanning electron microscopy (SEM), and statistical Raman spectroscopy of the as-grown and transferred materials.

Methods

Preparation

The 2D materials were grown via MOCVD on sapphire substrates in an AIXTRON cold-wall 2D R&D Close Coupled Showerhead (CSS[®]) reactor in 19 × 2" and 5 × 4" wafer configurations. We first developed a transfer process for cm-sized samples before scaling it to 100 mm wafers. First, polymethylmethacrylate (PMMA) 950k A6 was spin-coated onto the 2DMs to form an approximately 500 nm thick protection and support layer (see Fig. 1a, top). Second, the 2" wafers were cut with a diamond scriber to the desired size. The support frame was prepared from blue dicing tape 1008 R (70 μm polyvinyl chloride with a 10 μm acrylic adhesive layer) and surrounding plastic foil (commercially available printer foil, AVERY Zweckform GmbH) (see Fig. 1a, middle). The hole in the blue tape was smaller than the sapphire samples to attach the frame to the sapphire/2DM/PMMA stack (see Fig. 1a, bottom).

Transfer

The framed sample was then fixed with double-sided tape on a polyethylene terephthalate glycol (PETG) plastic cube with a defined surface angle of 10° inside a glass beaker (Fig. 1b, c, at the top). This angle was empirically determined to be optimal for 1.5 cm × 1.5 cm samples. We then filled the glass beaker with DI water until the water surface reached the sample. The surface tension of the DI water, supported by the hydrophobic behavior of

the dicing tape, caused the frame to float, transferring the surface tension force through the frame to the 2DM/PMMA stack (Fig. 1b, c, middle). The water eventually intercalated into the sapphire-2DM van der Waals gap, supported by the upward force of the frame, delaminating the 2DM from the sapphire. During delamination, we gradually filled the beaker with more water until the frame with the PMMA/2DM stack floated completely (Fig. 1b, c, bottom). The process time ranged from a few minutes to approximately half an hour, depending on the adhesion force between the 2DMs and the sapphire. The absence of bases or acids allows transfer without further decontamination steps.

Our target substrates were 2 × 2 cm silicon chips with 300 nm thermal silicon dioxide (SiO₂). A drop of DI water was placed onto the silicon chips. The frame with the 2DM was lifted from the DI water using tweezers, holding only the frame. Then, the 2DM was lowered onto the DI water drop, to which it adhered. This also flattened it upon contact, preventing the formation of cracks and wrinkles. The samples were dried at room temperature under laminar flow for one day. The frames were subsequently cut with a scalpel and removed. The PMMA/2DM stack remained on the target substrates, which were heated to 150 °C for 10 min to remove residual water and increase the adhesion of the 2DMs^{27–29}. Finally, the samples were placed in acetone for 3 h, rinsed in IPA, and heated under vacuum to 300 °C for 2 h to remove the PMMA. Optical microscope images of cm-scale h-BN and MoS₂ transferred onto 2 cm × 2 cm Si/SiO₂ chips are shown in Fig. 1e, f, respectively. Each image consists of 24 single microscope images stitched together, which leads to regular horizontal and vertical features, i.e., artifacts.

Results and discussion

We assessed the qualities of the h-BN and MoS₂ materials as-grown and after transfer via atomic force microscopy (AFM), Raman spectroscopy, and scanning electron microscopy (SEM). AFM was used in tapping mode to measure the surface topography of the materials. Raman spectroscopy can provide information on the layer number, defects, strain, and doping of 2DMs³⁰. Since the Raman signal of h-BN is weaker than that of MoS₂, we used a higher laser power and conducted fewer measurements for the former. We recorded 100 and 900 individual Raman spectra for h-BN and MoS₂, respectively, over a 10 μm × 10 μm area on both the as-grown and transferred materials. We used a laser with a wavelength of λ = 532 nm at powers of 20 mW (h-BN) and 1 mW (MoS₂) and an 1800 g/mm grating,

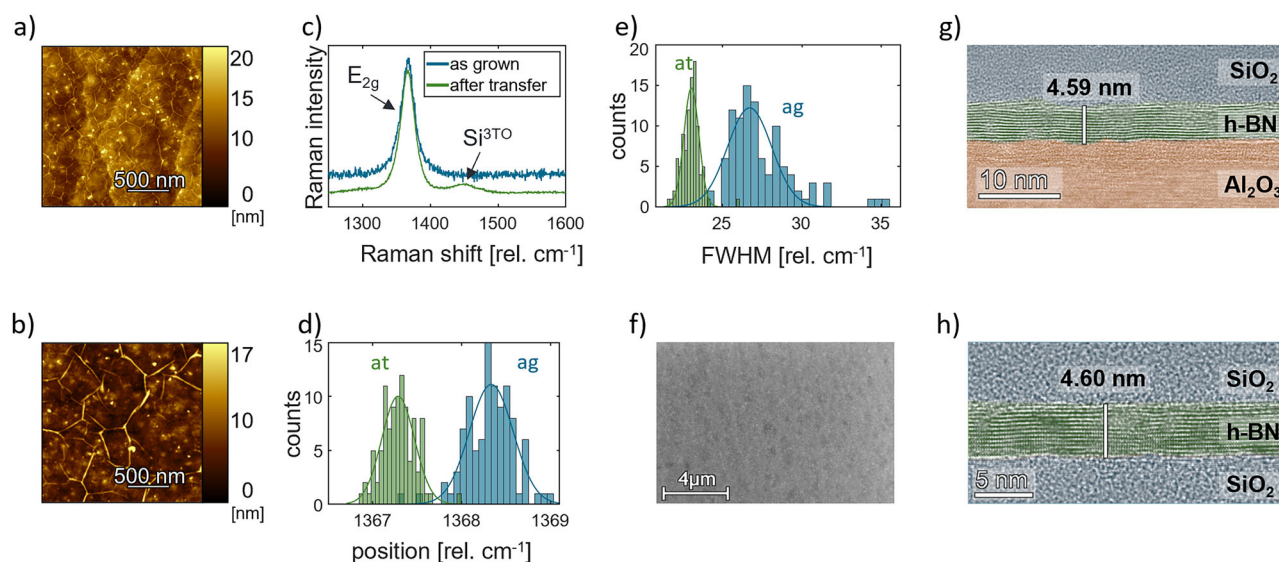


Fig. 2 | h-BN metrology as-grown and after transfer. **a** AFM measurement of the as-grown material with steps in the sapphire visible. **b** AFM measurement of the transferred material. **c** Raman spectra of h-BN as-grown and after transfer, with the characteristic E_{2g} peak in both spectra. The 3TO peak of the silicon substrate is also visible in the spectrum after transfer. **d** Histograms of the E_{2g} peak position of h-BN as-grown (ag, blue) and after transfer (at, green). **e** Respective histograms of the

FWHM of the characteristic peaks as-grown and after transfer. **f** Large-scale SEM image of the transferred h-BN on the Si/SiO₂ substrate. **g** Colored HRTEM image of the as-grown h-BN on sapphire encapsulated with SiO₂. An amorphous layer is visible between the crystalline Al₂O₃ and h-BN. The extracted h-BN thickness was 4.59 nm. **h** Colored HRTEM image of the transferred h-BN on SiO₂ encapsulated with SiO₂. The measured thickness was 4.60 nm.

resulting in a resolution of 0.3 cm^{-1} . The characteristic Raman peaks in every spectrum were fitted with Lorentz functions³¹. Additionally, we performed photoluminescence (PL) spectroscopy on both the as-grown and transferred MoS₂.

h-BN

An AFM topography scan of the as-grown h-BN revealed steps in the sapphire growth substrate formed at high temperatures (Fig. 2a), in line with a report in the literature³². In addition, wrinkles and particles are visible. After transfer, the h-BN appears smoother, which we attribute to the low RMS roughness of 360 pm of the thermally grown SiO₂ substrate (Fig. 2b). Wrinkles with the same periodicity as in the as-grown material vanish partially, while more pronounced wrinkles with larger periodicity appear. The rearrangement of wrinkles is possibly due to the release of growth-induced strain upon substrate change³³, while additional wrinkle formation during transfer cannot be fully excluded. The intrinsic strain in CVD h-BN is typically induced when the growth wafer is cooled to room temperature due to different thermal expansion coefficients of h-BN and sapphire. In contrast, wrinkles with a greater periodicity appear, which were likely formed during material transfer. The particle density remains unchanged.

The Raman spectra of the as-grown and transferred h-BN (Fig. 2c) both reveal the characteristic E_{2g} peak at $\sim 1368 \text{ cm}^{-1}$ ³⁴. An additional small peak appears at $\sim 1450 \text{ cm}^{-1}$ after transfer, identified as the 3TO peak from the silicon substrate³⁵. The statistical Raman analysis in Fig. 2d, e reveals a redshift of the peak position from 1368 cm^{-1} to 1367 cm^{-1} after transfer. Moreover, the FWHM decreased from 26.7 cm^{-1} to 23 cm^{-1} . The peak position of the as-grown material corresponds to mono- or bilayer h-BN, which contradicts the 14 ± 7 layers measured via AFM after transfer (compare Figures S1 and S2 in the supporting information) and the thickness of 4.6 nm extracted from TEM images (Fig. 2g, h). We attribute this peak position to the intrinsic strain in the material already observed as wrinkles in the AFM scan in Fig. 2a, which can easily lead to a slight redshift of the peak position³⁶. After transfer, the peak position of 1367 cm^{-1} is closer to the bulk value of 1366 cm^{-1} . The release of intrinsic stress can also explain the decrease in the FWHM after transfer³⁷. Doping or defects typically lead to an increase in the FWHM³⁸. Thus, we conclude that our transfer process increases the quality in terms of the FWHM of the Raman signal.

Wrinkles on the h-BN surface are also visible in the SEM image after transfer (Fig. 2f, reproduced, larger version in supporting information Figure. S3) with the same periodicity as those observed in the AFM measurement (Fig. 2b). They appear as bright lines against a gray background. Dirt or PMMA residues appear as small bright spots within the image. These bright spots are only faintly visible in the SEM image because of their low particle density and small size, typically a few tens of nanometers, which supports the results of the AFM measurement in Fig. 2b.

We performed high-resolution transmission electron microscopy (HRTEM) on cross sections of both the as-grown (Fig. 2g) and the transferred h-BN (Fig. 2h) samples to measure the thickness with atomic resolution and clarify the contradictory AFM thickness and Raman measurements discussed earlier. Both samples were encapsulated in evaporated SiO₂ prior to lamella preparation to protect the h-BN. In Fig. 2g, the layered structure of the h-BN (green) is clearly visible, positioned between the crystalline Al₂O₃ (orange) and the protective SiO₂ (blue). An amorphous layer between the h-BN and the crystalline Al₂O₃ is visible, which is likely amorphized Al₂O₃³⁹ or an aluminum-nitride compound formed during the growth process⁴⁰. We measure a thickness of the as-grown h-BN of 4.59 nm, consistent with our AFM thickness measurement after transfer (see supporting information Figures S1 and S2). Thus, we conclude that the Raman peak shift of the as-grown h-BN at $\sim 1368 \text{ cm}^{-1}$ is indeed due to intrinsic strain. In Fig. 2h, the transferred h-BN (green) is sandwiched between the SiO₂ of the target substrate and the protective SiO₂ (blue). The layered structure of the h-BN is preserved, and no significant defects are visible. HRTEM revealed no PMMA or other contaminants at the interfaces of the h-BN. Notably, we measured the same h-BN thickness of 4.6 nm as that of the as-grown material. Overall, the HRTEM analysis revealed no significant degradation or material loss during the transfer process.

MoS₂

AFM scans in Fig. 3a, b show the nanocrystallinity of MoS₂. They also reveal the presence of contamination particles (bright spots) and vertical nanosheets (bright lines), a typical byproduct of thick MoS₂ growth⁴¹. The nanocrystalline structure of MoS₂ remained after transfer, and the number of particles increased slightly.

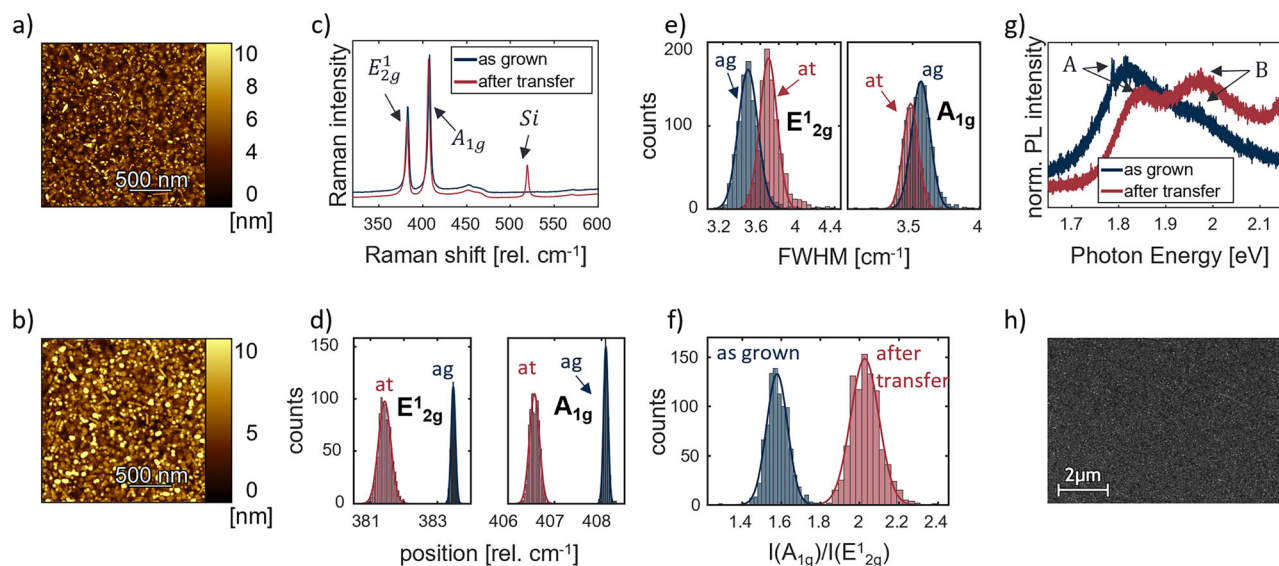


Fig. 3 | MoS₂ metrology as-grown and after transfer. **a** AFM measurement of the as-grown material. **b** AFM measurement after transfer. **c** Raman spectra of MoS₂ as-grown and after transfer, with characteristic E_{2g}¹ and A_{1g} peaks visible in both spectra. **d** Histograms of the E_{2g}¹ and A_{1g} peak positions of MoS₂ as-grown (ag, red)

and after transfer (at, blue). **e** Respective histograms of the FWHM of the characteristic peaks as-grown (ag) and after transfer (at). **f** Histogram of the I(A_{1g})/I(E_{2g}¹) intensity ratios. **g** PL spectra of MoS₂ as-grown and after transfer. **h** SEM image of the transferred MoS₂ on the Si/SiO₂ substrate.

The Raman analysis results as-grown and after transfer are shown in Fig. 3c–f. Two exemplary spectra as-grown and after transfer (Fig. 3c) reveal the characteristic E_{2g}¹ and A_{1g} peaks of MoS₂ at 383 cm⁻¹ and 408 cm⁻¹, respectively⁴². The spectrum after transfer also shows the characteristic peak of the silicon substrate at 520 cm⁻¹. Histograms of the Raman peak positions and full width at half maximum (FWHM) values from MoS₂ as-grown (ag) and after transfer (at) are shown in Fig. 3d, e. A Gaussian distribution function fitted to the histograms revealed a slight redshift of both the E_{2g}¹ and A_{1g} peaks (Fig. 3d) by approximately 2 cm⁻¹ and 1.5 cm⁻¹, respectively. The FWHM of the E_{2g}¹ peak increased from 3.5 cm⁻¹ to 3.7 cm⁻¹ after transfer. In contrast, the FWHM of the A_{1g} peak decreased from 3.6 cm⁻¹ to 3.5 cm⁻¹ (compare Fig. 3e). These changes lie within the error margins of our measurement setup (0.41 cm⁻¹ for the FWHM calculation; see supporting information section S1), and we conclude that there is no detectable change due to transfer. The intensity ratio of the A_{1g} peak to the E_{2g}¹ peak increases from 1.57 to 2.03 after transfer, or 28.4%. The photoluminescence (PL) data as-grown and after transfer in Fig. 3g show a slight blueshift of the excitonic A and B peaks. The B peak is more pronounced after transfer than during the measurement of the as-grown material.

The shift in the characteristic peak positions in the Raman and PL spectra and the increase in the I(A_{1g})/I(E_{2g}¹) intensity ratio indicate a change in the material properties due to transfer. In MoS₂, the number of layers, material strain, doping, and defects influence the characteristic peak positions^{30,42,43}. We measured a thickness of 7.1 ± 1.4 nm of the MoS₂ after transfer via AFM at the edge of a transferred film (Figures S4 and S5 in the supporting information), which corresponds to 11 ± 2 layers⁴⁴. The extracted characteristic peak positions and the I(E_{2g}¹)/I(A_{1g}) ratio of 0.5 support the finding of the AFM edge scan, as it indicates bulk material behavior⁴³. The Raman peaks are influenced by the number of layers only up to ~ seven layers, whereas they converge to bulk material behavior for thicker materials⁴³. Therefore, we do not expect any influence of a possible change in the number of MoS₂ layers on the Raman signals. The redshift of the two peaks after transfer indicates an increase in the tensile biaxial strain inside the material^{30,45–47}. An increase in the I(A_{1g})/I(E_{2g}¹) ratio indicates either a decrease in the biaxial compression strain or tensile strain⁴⁸. One potential explanation for our findings is that the initial compression strain of the as-grown material is partially released in the transferred material. The shift of the A peak in the PL spectrum supports a change in the intrinsic strain of the material⁴⁶. The doping of a material with excess charge

influences the A_{1g} peak position and FWHM⁴², which we do not observe here. Our PL signal reveals less quenching of the B peak and a blueshift of the A peak, indicating less n-doping after transfer. We attribute this to the substrate change from Al₂O₃ (growth substrate) to SiO₂ (target substrate). Al₂O₃ in the vicinity of MoS₂ often leads to n-type doping because of positive fixed charges at the Al₂O₃ interface⁴⁹. These changes manifest as a redshift of the A peak and quenching of the B peak in the PL signal^{50,51}. The absence of Al₂O₃ after transfer leads to the opposite behavior of the PL signal.

The characteristic Raman peak positions are also influenced by lattice defects, i.e., an increase in the defect density leads to a redshift of the E_{2g}¹ peak and a (comparably smaller) blueshift of the A_{1g} peak³⁰. At the same time, the FWHM of the peaks increases³⁰. We exclude a significant increase in the defect density because there is no blueshift of the A_{1g} peak and no significant increase in the FWHM of the peaks.

The SEM image of the transferred MoS₂ in Fig. 3h confirms the presence of contamination particles (bright spots) and vertical growth walls (lines), which are also visible in the AFM data. We did not observe macroscopic polymer residues or cracks. A reproduced, larger version of the SEM image can be found in the supporting information in Figure. S6.

In summary, the analysis of the Raman and PL spectra revealed no significant degradation in material quality but a decrease in compressive strain after transfer. Notably, the reduction in compressive strain aligns with the results of the h-BN transfer. We observed a slight increase in the number of particles on the transferred film in the AFM scans, likely due to PMMA contamination.

We compared our DI water-based method with KOH-based delamination processes typically used for MoS₂^{17,50,52}. MoS₂ samples with an area of 1.5 × 1.5 cm² were transferred from a single sapphire wafer following the procedure of our method (see microscope images in Figure. S7 in the supporting information) using either an aqueous KOH solution with a concentration of 4 M or DI water for delamination. Due to the corrosive nature of KOH, the KOH-transferred samples were subsequently cleaned by floating on a DI water surface for three days, whereas the DI water-transferred samples were directly attached to the target Si/SiO₂ substrates. All subsequent sample preparation steps were identical and followed the prescribed procedure. The MoS₂ transferred using DI water exhibited similar Raman peak shifts as discussed previously, with an indication of partial intrinsic stress release during the transfer. In contrast, we observed a

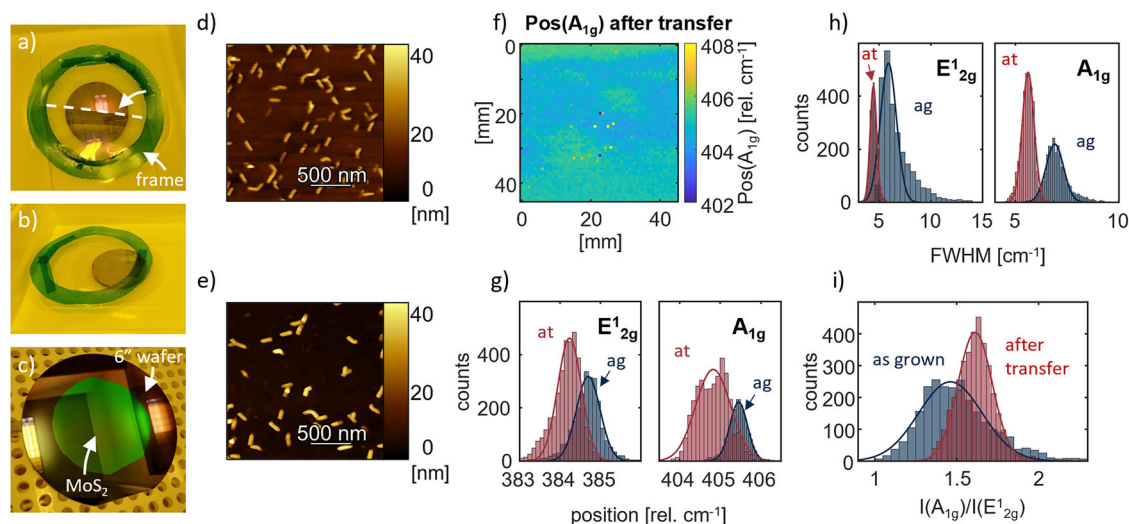


Fig. 4 | 100 mm MoS₂ wafer transfer and corresponding material analysis as and after transfer. **a** Photograph taken during the delamination process. The dashed line indicates the propagation line of delamination from the sapphire substrate. **b** Photograph of delaminated MoS₂ floating on DI water. The sapphire substrate can be seen remaining on the socket. **c** Photograph of transferred MoS₂ on an oxidized 150 mm Si wafer. **d** AFM measurement of the as-grown material. **e** AFM

measurement after transfer. **f** Color map of the characteristic A_{1g} Raman peak position after transfer of a 45 mm × 45 mm area. **g** Histograms of the E_{12g}¹ and A_{1g} peak positions of MoS₂ as-grown (ag, blue) and after transfer (at, red). **h** Histograms of the FWHMs of the Raman peaks as-grown and after transfer. **i** Histograms of the respective I(A_{1g})/I(E_{12g}¹) intensity ratios.

slight blueshift of the E_{12g}¹ peak and no significant A_{1g} peak shift after the KOH-based transfer (supporting information Figure. S8a). This behavior was already reported by A. P. Singh et al.¹⁶ and attributed to partial oxidation and dissolution of MoS₂ in a base solution. AFM scans revealed no significant difference between the MoS₂ transferred using DI water and using a KOH solution (SI Figure. S9). However, in both cases, a slight increase in particle contamination was observed after the transfer.

Scalability

We demonstrated the scalability of the method through the wafer-scale transfer of MoS₂ grown on a 100 mm sapphire wafer. The wafer was prepared like the samples: first, an approximately 500 nm thick PMMA film was spin-coated as a supporting film. Second, a round-shaped frame was prepared (see Fig. 4a). The framed wafer was fixed with double-sided tape onto a PETG socket placed on the ground of a 20 cm × 30 cm plastic tub. We used a round socket with a diameter of 60 mm and an angle of 5° instead of 10° because of the larger size of the MoS₂ wafer.

The delamination of MoS₂ was carried out in the same manner as for the smaller samples. Photographs of different stages of transfer are presented in Fig. 4a–c. In Fig. 4a, approximately half of the MoS₂ is detached from the growth substrate, as visible by a different reflection of the light on the wafer in the lower half compared with that in the upper half. The white dashed line indicates the propagation line of delamination from the growth substrate. Once MoS₂ was completely detached from the growth substrate, it floated on the water surface (Fig. 4b).

The wet transfer of MoS₂ differs at this point from that of the small samples, as it is too unstable to be safely removed from the water. Instead, we used a “fishing method”: the target substrate, a Si wafer with 300 nm thermally oxidized SiO₂, was submerged in the water, moved below the MoS₂/PMMA stack, and carefully extracted from the DI water at an angle, “fishing” the stack onto the SiO₂ surface. The frame helped to handle and stabilize the 2DM/PMMA stack on the water surface. The transferred material subsequently underwent the same process of drying, PMMA removal, and annealing as the smaller samples did.

Raman and AFM measurements were taken as-grown and after transfer. The results are shown in Fig. 4d–i. An AFM scan of a 2 μm × 2 μm area of the as-grown material (Fig. 4d) reveals many vertical nanosheets that likely formed during material growth⁴¹. These are visible

as bright lines in the AFM image. The vertical nanosheets are thicker (~90 nm vs. ~20 nm) and higher (~8 nm vs. ~30 nm) compared to the MoS₂ used for the cm-scale transfer (Fig. 3a) due to different growth processes. A comparison of the AFM measurements as-grown (Fig. 4d) and after the transfer (Fig. 4e) indicates a lower density of vertical nanosheets after the transfer, likely because of the different measurement positions before and after the transfer. More importantly, no contamination or cracks are visible after transfer.

Figure 4f shows a color map of the A_{1g} peak positions after MoS₂ transfer of 60 × 60 Raman spectra over an area of 45 mm × 45 mm, exhibiting a largely homogeneous region with a few missing spots (dark blue and yellow pixels in the center) where no Raman signal of the MoS₂ could be observed. A color map of the E_{12g}¹ peak position can be found in the supporting information Figure. S10c. Notably, this color map also contains missing spots that are not at the same positions as those in Fig. 4f. Thus, some of the missing spots may arise from fitting failures and some may arise from defects in the material introduced during transfer. However, with only ~10 missing pixels out of 3600, the proven MoS₂ coverage remains high at approximately 99.7%. The corresponding large-area Raman scans of the as-grown material can be found in the supporting information Figure. S10a and S10b.

Figure 4g–i show histograms of the peak positions, the FWHM, and the intensity ratio of the characteristic E_{12g}¹ and A_{1g} peaks as-grown and after transfer. The results are similar to the results of the MoS₂ transfer of the smaller samples (Fig. 3d–f). A redshift of the E_{12g}¹ and A_{1g} peaks by 0.5 cm⁻¹ and 0.7 cm⁻¹, respectively, is observed due to the transfer (Fig. 4g). The FWHMs of the E_{12g}¹ and A_{1g} peaks decrease by 1.5 cm⁻¹ and 1.3 cm⁻¹, respectively, after transfer (Fig. 4h). The I(A_{1g})/I(E_{12g}¹) ratio slightly increases from 1.5 to 1.6 after transfer. Both findings indicate a reduction of compressive strain in the material^{42,45,48}, similar to the small sample transfer, showcasing the reproducibility of the method. However, further comparisons of the quality of both materials are not meaningful, as they were synthesized via different growth processes.

We used the transfer method in independent studies to fabricate electronic devices, including back- and top-gated MoS₂ field effect transistors (FETs)⁵³, lateral and vertical MoS₂ memristors^{54–56}, and vertical h-BN memristors⁵⁷. The electrical device data can be found in the corresponding works.

Table S3 in the supporting information summarizes commonly used transfer techniques for 2D transition metal dichalcogenides (TMDCs) and h-BN to place the proposed transfer method in the context of established approaches. The methods are compared based on a qualitative assessment of their key characteristics, including required chemicals, typical transfer size, contamination level after transfer, scalability, and reported advantages and limitations. Notably, many works present centimeter-scale or sample-size transfers, and scalability is often not addressed. Additionally, polymer-related contamination after transfer remains an open issue in the field. Possible solutions include the use of sacrificial water-soluble support layers, as presented for MoS₂ in ref. 58, and for graphene grown on Cu foil in refs. 59,60. Such approaches applied to our method could reduce polymer residues after transfer and, in principle, eliminate the need for chemicals other than DI water and the carrier polymer.

Applicability to other 2DM/ substrate systems

Based on the theoretical concept proposed by Zhang et al.²², the peeling of a 2DM from a substrate using DI water should, in principle, be possible whenever both surfaces are hydrophilic. However, the hydrophilicity of 2DMs depends on several factors, including the number of layers, surface defects, atomic edges, and the growth substrate^{26,61}. For instance, ideal, defect-free h-BN is expected to be hydrophobic, whereas h-BN with atomic edges is hydrophilic²⁶. Si/SiO₂ substrates, which are also commonly used for 2DM growth, showed WCAs ranging from 21° to 40°^{62,63}, indicating strong hydrophilicity. Copper (Cu) foils, another widely used growth substrate for 2DMs, exhibit a broad range of WCAs, from about 32° to values exceeding 100°, depending on crystallographic orientation and surface contamination, such as hydrocarbons introduced by air exposure^{64,65}.

Beyond wettability, the substrate's mechanical stability is a critical factor in the transfer process. Rigid substrates such as sapphire and Si/SiO₂ can be readily fixed to the transfer socket, enabling controlled peeling and handling. In contrast, flexible substrates like Cu foils may wrinkle during fixation, potentially damaging both the 2DM and the PMMA protective layer. 2DMs grown on Cu foil are commonly transferred by etching the Cu substrate in corrosive solution^{66,67}.

In conclusion, we demonstrate a DI water-based, large-scale transfer method for the 2DMs h-BN and MoS₂ grown with scalable MOCVD processes on sapphire substrates. The surface tension of DI water is used to delaminate the 2DMs from the sapphire via a supporting frame. No chemicals, such as KOH or other etchants, were used for the transfer. The material qualities as-grown and after transfer were compared via AFM and SEM measurements as well as statistical Raman analysis. The Raman measurements revealed a reduction of intrinsic compressive strain due to the transfer of the materials from the growth substrate to the target substrate. In addition, no significant material degradation was observable. AFM images of h-BN revealed no increase in the particle density after transfer. HRTEM images confirmed that the h-BN thickness was preserved during transfer and showed no residues after transfer. AFM measurements of MoS₂ revealed a slight increase of nanometer-sized particles on the material after transfer. We demonstrated the scalability of our water-based, frame-assisted transfer process toward industry-relevant wafer sizes with the transfer of MoS₂ from a 100 mm diameter sapphire wafer to a 150 mm Si/SiO₂ wafer. Like for the smaller samples, large-scale Raman mapping reveals no significant quality degradation but an intrinsic stress release after transfer.

Data availability

The authors declare that all data supporting the findings and conclusions of this work can be found in the article and supplementary information. Additional data relating to this study is available upon reasonable request by the corresponding author.

Received: 5 September 2025; Accepted: 7 April 2026;

Published online: 20 April 2026

References

- Koppens, F. H. L. et al. Photodetectors based on graphene, other two-dimensional materials and hybrid systems. *Nat. Nanotechnol.* **9**, 780–793 (2014).
- Ferrari, A. C. et al. Science and technology roadmap for graphene, related two-dimensional crystals, and hybrid systems. *Nanoscale* **7**, 4598–4810 (2015).
- Akinwande, D. et al. Graphene and two-dimensional materials for silicon technology. *Nature* **573**, 507–518 (2019).
- Chen, S. et al. Wafer-scale integration of two-dimensional materials in high-density memristive crossbar arrays for artificial neural networks. *Nat. Electron.* **3**, 638–645 (2020).
- Lemme, M. C. et al. Nanoelectromechanical sensors based on suspended 2D materials. *Research*. <https://doi.org/10.34133/2020/8748602> (2020).
- Yao, J. D. & Yang, G. W. All-2D architectures toward advanced electronic and optoelectronic devices. *Nano Today* **36**, 101026 (2021).
- Lemme, M. C., Akinwande, D., Huyghebaert, C. & Stampfer, C. 2D materials for future heterogeneous electronics. *Nat. Commun.* **13**, 1392 (2022).
- Kim, J., Ju, X., Ang, K.-W. & Chi, D. Van der Waals layer transfer of 2D materials for monolithic 3D electronic system integration: review and outlook. *ACS Nano* **17**, 1831–1844 (2023).
- Zhu, J. et al. Low-thermal-budget synthesis of monolayer molybdenum disulfide for silicon back-end-of-line integration on a 200 mm platform. *Nat. Nanotechnol.* **18**, 456–463 (2023).
- Xie, J. et al. On-chip direct synthesis of boron nitride memristors. *Nat. Nanotechnol.* **20**, 1596–1604 (2025).
- Krishna, S., Choi, S. H., Kim, S. M. & Kim, K. K. Sapphire substrates for large-area 2D transition metal dichalcogenides synthesis: a brief review. *Curr. Appl. Phys.* **59**, 208–213 (2024).
- Li, T. et al. Epitaxial growth of wafer-scale molybdenum disulfide semiconductor single crystals on sapphire. *Nat. Nanotechnol.* **16**, 1201–1207 (2021).
- Zhu, H. et al. Step engineering for nucleation and domain orientation control in WSe₂ epitaxy on c-plane sapphire. *Nat. Nanotechnol.* **18**, 1295–1302 (2023).
- Nakamura, S. & Krames, M. R. History of gallium-nitride-based light-emitting diodes for illumination. *Proc. IEEE* **101**, 2211–2220 (2013).
- Bhuyan, C. A. et al. A novel methodology of using nonsolvent in achieving ultraclean transferred monolayer MoS₂. *Adv. Mater. Interfaces* **9**, 2200030 (2022).
- Singh, A. P. et al. Unravelling chemical etchant influences during assisted wet-transfer to obtain high quality MoS₂ atomic layers. *Appl. Surf. Sci.* **669**, 160331 (2024).
- Schneider, D. S. et al. Highly responsive flexible photodetectors based on MOVPE grown uniform few-layer MoS₂. *ACS Photonics* **7**, 1388–1395 (2020).
- Amani, M. et al. Growth-substrate induced performance degradation in chemically synthesized monolayer MoS₂ field effect transistors. *Appl. Phys. Lett.* **104**, 203506 (2014).
- Anichini, C. et al. Chemical sensing with 2D materials. *Chem. Soc. Rev.* **47**, 4860–4908 (2018).
- Lee, C. W., Suh, J. M. & Jang, H. W. Chemical sensors based on two-dimensional (2D) materials for selective detection of ions and molecules in liquid. *Front. Chem.* **7**, 708 (2019).
- Mackin, C. et al. Chemical sensor systems based on 2D and thin film materials. *2D Mater.* **7**, 022002 (2020).
- Zhang, Y., Liu, Q. & Xu, B. Liquid-assisted, etching-free, mechanical peeling of 2D materials. *Extrem. Mech. Lett.* **16**, 33–40 (2017).
- Law, K.-Y. Definitions for hydrophilicity, hydrophobicity, and superhydrophobicity: getting the basics right. *J. Phys. Chem. Lett.* **5**, 686–688 (2014).

24. Leem, J. W. & Yu, J. S. Wafer-scale highly-transparent and superhydrophilic sapphires for high-performance optics. *Opt. Express* **20**, 26160–26166 (2012).
25. Wang, E. et al. Water nanolayer facilitated solitary-wave-like blisters in MoS₂ thin films. *Nat. Commun.* **14**, 4324 (2023).
26. Feng, Z. et al. Anisotropic interfacial force field for interfaces of water with hexagonal boron nitride. *Langmuir* **39**, 18198–18207 (2023).
27. Zheng, F. et al. Critical stable length in wrinkles of two-dimensional materials. *ACS Nano* **14**, 2137–2144 (2020).
28. Megra, Y. T., Lim, S., Lim, T., Na, S. R. & Suk, J. W. Enhancement of the adhesion energy between monolayer graphene and SiO₂ by thermal annealing. *Appl. Surf. Sci.* **570**, 151243 (2021).
29. Schätz, J. et al. Button shear testing for adhesion measurements of 2D materials. *Nat. Commun.* **15**, 2430 (2024).
30. Tumino, F., D'Agosta, P., Russo, V., Li Bassi, A. & Casari, C. S. Raman spectroscopy of 2D MoS₂ interacting with metals. *Crystals* **13**, 1271 (2023).
31. Dieing, T., Hollricher, O. & Toporski, J. (eds) *Confocal Raman Microscopy* (Springer Berlin Heidelberg, 2011).
32. Biswas, A. et al. Unidirectional domain growth of hexagonal boron nitride thin films. *Appl. Mater. Today* **30**, 101734 (2023).
33. Yang, X. et al. Growth of hexagonal boron nitride on sapphire substrate by pulsed-mode metalorganic vapor phase epitaxy. *J. Cryst. Growth* **482**, 1–8 (2018).
34. Li, L. H., Cervenka, J., Watanabe, K., Taniguchi, T. & Chen, Y. Strong oxidation resistance of atomically thin boron nitride nanosheets. *ACS Nano* **8**, 1457–1462 (2014).
35. Spizzirri, P. G., Fang, J. H., Rubanov, S., Gauja, E. & Prawer, S. Nano-Raman spectroscopy of silicon surfaces. <https://doi.org/10.48550/ARXIV.1002.2692> (2010).
36. Zhang, G., Chang, Y. & Yan, B. The study of the wrinkles of hexagonal boron-nitride flake after the annealing. *Crystals* **13**, 304 (2023).
37. Gorbachev, R. V. et al. Hunting for monolayer boron nitride: optical and Raman signatures. *Small* **7**, 465–468 (2011).
38. Stehle, Y. et al. Synthesis of hexagonal boron nitride monolayer: control of nucleation and crystal morphology. *Chem. Mater.* **27**, 8041–8047 (2015).
39. Bansal, A. et al. Substrate modification during chemical vapor deposition of hBN on sapphire. *ACS Appl. Mater. Interfaces* **13**, 54516–54526 (2021).
40. Chugh, D. et al. Flow modulation epitaxy of hexagonal boron nitride. *2D Mater.* **5**, 045018 (2018).
41. Li, H., Wu, H., Yuan, S. & Qian, H. Synthesis and characterization of vertically standing MoS₂ nanosheets. *Sci. Rep.* **6**, 21171 (2016).
42. Iqbal, M. W., Shahzad, K., Akbar, R. & Hussain, G. A review on Raman finger prints of doping and strain effect in TMDCs. *Microelectron. Eng.* **219**, 111152 (2020).
43. Chakraborty, B., Matte, H. S. S. R., Sood, A. K. & Rao, C. N. R. Layer-dependent resonant Raman scattering of a few layer MoS₂. *J. Raman Spectrosc.* **44**, 92–96 (2013).
44. Zhao, Y. & Ouyang, G. Thickness-dependent photoelectric properties of MoS₂/Si heterostructure solar cells. *Sci. Rep.* **9**, 17381 (2019).
45. Conley, H. J. et al. Bandgap engineering of strained monolayer and bilayer MoS₂. *Nano Lett.* **13**, 3626–3630 (2013).
46. Lloyd, D. et al. Band gap engineering with ultralarge biaxial strains in suspended monolayer MoS₂. *Nano Lett.* **16**, 5836–5841 (2016).
47. Kataria, S. et al. Growth-induced strain in chemical vapor deposited monolayer MoS₂: experimental and theoretical investigation. *Adv. Mater. Interfaces* **4**, 1700031 (2017).
48. Kukucska, G. & Koltai, J. Theoretical investigation of strain and doping on the Raman spectra of monolayer MoS₂. *Phys. Status Solidi B* **254**, 1700184 (2017).
49. Illarionov, Y. Y. et al. Insulators for 2D nanoelectronics: the gap to bridge. *Nat. Commun.* **11**, 1–15 (2020).
50. Piacentini, A. et al. Stable Al₂O₃ Encapsulation of MoS₂-FETs Enabled by CVD grown h-BN. *Adv. Electron. Mater.* **8**, 2200123 (2022).
51. Kim, S. Y., Yang, H. I. & Choi, W. Photoluminescence quenching in monolayer transition metal dichalcogenides by Al₂O₃ encapsulation. *Appl. Phys. Lett.* **113**, 133104 (2018).
52. Najmaei, S. et al. Vapour phase growth and grain boundary structure of molybdenum disulphide atomic layers. *Nat. Mater.* **12**, 754–759 (2013).
53. Esteki, A. et al. Tunable doping and mobility enhancement in 2D channel field-effect transistors via damage-free atomic layer deposition of AlOX dielectrics. <https://doi.org/10.48550/arXiv.2408.07183> (2024).
54. Cruces, S. et al. Volatile and nonvolatile resistive switching in lateral 2D molybdenum disulfide-based memristive devices. *Nano Lett.* <https://doi.org/10.1021/acs.nanolett.5c01992> (2025).
55. Ran, K. et al. Unraveling the dynamics of conductive filaments in MoS₂-based memristors by operando transmission electron microscopy. *Nat. Commun.* **16**, 7433 (2025).
56. Lee, J. et al. Integration of low-voltage nanoscale MoS₂ memristors on CMOS microchips. <https://doi.org/10.5281/zenodo.17860830> (2025).
57. Völkel, L. et al. Influence of humidity on the resistive switching of hexagonal boron nitride-based memristors. *Npj 2D Mater. Appl.* **9**, 41 (2025).
58. Zhang, L. et al. Damage-free and rapid transfer of CVD-grown two-dimensional transition metal dichalcogenides by dissolving sacrificial water-soluble layers. *Nanoscale* **9**, 19124–19130 (2017).
59. Yallow, T. B. et al. Effects of the transfer method and interfacial adhesion on the frictional and wear resistance properties of a graphene-coated polymer. *Nanomaterials* **13**, 655 (2023).
60. Narute, P. et al. Structural integrity preserving and residue-free transfer of large-area wrinkled graphene onto polymeric substrates. *ACS Nano* **16**, 9871–9882 (2022).
61. Snapp, P. et al. Interaction of 2D materials with liquids: wettability, electrochemical properties, friction, and emerging directions. *NPG Asia Mater.* **12**, 22 (2020).
62. Geistlinger, H. et al. Evaporation study based on micromodel experiments: comparison of theory and experiment. *Water Resour. Res.* **55**, 6653–6672 (2019).
63. Bryk, P. et al. What is the value of water contact angle on silicon? *Materials* **13**, 1554 (2020).
64. Korczeniewski, E. et al. Revisiting wetting, freezing, and evaporation mechanisms of water on copper. *ACS Appl. Mater. Interfaces* **13**, 37893–37903 (2021).
65. Löblein, S. M., Merz, R., Müller, D. W., Kopnarski, M. & Mücklich, F. The influence of adventitious carbon groups on the wetting of copper: a study on the effect of microstructure on the static contact angle. *Langmuir* **39**, 12020–12031 (2023).
66. Rademacher, N. et al. CVD graphene-MoS₂ Van der Waals heterostructures on the millimeter-scale. *Micro Nano Eng.* **23**, 100256 (2024).
67. Cheliotis, I. & Zergioti, I. A review on transfer methods of two-dimensional materials. *2D Mater.* **11**, 022004 (2024).

Acknowledgements

We gratefully acknowledge financial support from the German Federal Ministry of Research, Technology and Space (BMFT) within the projects NEUROTEC 2 (16ME0399, 16ME0400), NeuroSys 2 (03ZU2106AA, 03ZU2106AE, 03ZU2106AD) and nanodiag BW (03ZU1208BC, 03ZU1208BB), and the German Research Foundation (DFG) under the projects 2D-NEMS (LE 2440/11-1) and TRR 404 Active-3D (528378584). We acknowledge funding from the European Union's Horizon Europe research and innovation program (via CHIPS-JU) under the project ENERGIZE (101194458). The views and opinions expressed are those of the authors only and do not necessarily reflect those of the European Union or the

European Commission. Neither the European Union nor the European Commission can be held responsible for them. Open Access funding enabled and organized by Projekt DEAL. The authors acknowledge support from StrucMatLab, RWTH Aachen University.

Author contributions

The experiments were conceived by N.R., L.V., E.R., M.O., and M.C.L. The 2D material growth was conceived and carried out by S.K., J.M., E.Y., C.M., A.H., and M.H. The 2DM was conducted and performed by N.R. and L.V. Raman, AFM, and SEM measurements and their analysis were performed by N.R., and L.V. The TEM measurements were performed by K.R. and J.M. All authors collaborated on the interpretation of the experiments. The manuscript was written and revised by all. The work was supervised by M.C.L.

Funding

Open Access funding enabled and organized by Projekt DEAL.

Competing interests

M.C.L. is the managing director and N.R., M.O., and K.R. are employees of the non-profit company AMO gGmbH, whereas S.K., J.M., E.Y., C.M., A.H., and M.H. are employees of AIXTRON SE. Both companies are partners of several publicly funded research projects and are working on the growth and device integration of 2D materials. L.V., E.R., and J.M. have no competing interests.

Additional information

Supplementary information The online version contains supplementary material available at <https://doi.org/10.1038/s41699-026-00696-z>.

Correspondence and requests for materials should be addressed to Max C. Lemme.

Reprints and permissions information is available at <http://www.nature.com/reprints>

Publisher's note Springer Nature remains neutral with regard to jurisdictional claims in published maps and institutional affiliations.

Open Access This article is licensed under a Creative Commons Attribution 4.0 International License, which permits use, sharing, adaptation, distribution and reproduction in any medium or format, as long as you give appropriate credit to the original author(s) and the source, provide a link to the Creative Commons licence, and indicate if changes were made. The images or other third party material in this article are included in the article's Creative Commons licence, unless indicated otherwise in a credit line to the material. If material is not included in the article's Creative Commons licence and your intended use is not permitted by statutory regulation or exceeds the permitted use, you will need to obtain permission directly from the copyright holder. To view a copy of this licence, visit <http://creativecommons.org/licenses/by/4.0/>.

© The Author(s) 2026